

The NIST EOS thermal-infrared transfer radiometer

J. P. Rice and B. Carol Johnson

Abstract. A portable thermal-infrared transfer radiometer (TXR) has been developed for use in comparisons and scale verifications of sources used to calibrate thermal-infrared (TIR) channels of the National Aeronautics and Space Administration's (NASA's) Earth Observing System (EOS) flight instruments. The TXR is designed to measure the radiance temperature of large-area black-body sources in cryogenic vacuum environments, either at the National Institute of Standards and Technology (NIST) or at the EOS instrument-calibration facilities. It can be operated in ambient conditions of room temperature and pressure, or in EOS instrument thermal/vacuum chambers at temperatures as low as 77 K. The TXR is a liquid-nitrogen-cooled filter radiometer with two channels: one centred at 5 μm based on a photovoltaic InSb detector, and the other centred at 10 μm based on a photovoltaic HgCdTe (MCT) detector. The spectral, spatial and temporal characterization of the TXR using state-of-the-art NIST ambient-infrared instrumentation is reported.

1. Introduction

A programme to establish radiometric traceability between NASA's EOS instrument-calibration facilities and the NIST radiance scale is underway [1-3]. As part of this programme, the NIST will provide a portable radiometer, the TXR, for NIST-traceable radiometric comparisons between the cryogenic black-body working standard sources used for EOS TIR calibrations in several different thermal-vacuum calibration facilities [4-6].

This paper describes the design and characterization of the TXR. Most of the EOS calibration facility working standards are cavity-type black bodies having aperture sizes ranging from 4 cm to 10 cm and a radiance temperature in the range 200 K to 400 K. Typical values reported for the calculated effective emissivity are, for example, 0.9997 [4] or 0.999 952 [7]. The working standard radiance scales are generally based on models that use the Planck radiation formula with modelled emissivity and temperature uniformity and the measured contact temperature of the NIST-traceable platinum resistance thermometers (PRTs) affixed to the cavity walls. The estimated uncertainty in the radiance temperature from such models is typically about 0.05 % [7]. Thus, the TXR is designed to enable radiometric comparisons to verify that the radiance temperature scales are within 0.05 % of each other, as the uncertainty estimates predict. Furthermore, rather than relying on a scale based on contact thermometry alone for calibration of the TXR at the NIST, the

TXR can be calibrated against the NIST detector-based radiometric scale. This scale uses electrical-substitution radiometry to measure radiant power traceable to electrical scales [8]. As such, the TXR provides a means of absolute calibration independent of the problems associated with estimating the uncertainty of the contact-thermometry-based radiance temperature of a black-body source. In fact, new developments at the NIST will eventually enable the TXR to be calibrated absolutely without involving a black-body source [9].

2. TXR design

The TXR is a two-channel filter radiometer based on liquid-nitrogen-cooled semiconductor photodiode detectors. Channel 1 uses a photovoltaic InSb detector with a filter that has a nominal centre wavelength of 5 μm , and Channel 2 uses a photovoltaic HgCdTe (MCT) detector with a filter that has a nominal centre wavelength of 10 μm . For both channels, the nominal bandwidth is 1 μm .

The TXR is packaged in a portable liquid-nitrogen cryostat, which consists of a liquid-nitrogen reservoir, a cold plate, and a radiation shield thermally isolated from an outer vacuum shell. The cold plate forms the bottom of the nitrogen reservoir, such that its top surface is in contact with liquid nitrogen while its bottom surface is under vacuum and has a set of blind-tapped holes for mounting the various TXR components. Figure 1 shows the optical layout of these components, as viewed from the bottom of the cryostat. The inside of the aluminium radiation shield and the baffles are painted with a diffuse infrared-black paint. The radiation shield mounts onto the cold plate and encloses the components on the cold plate, allowing light to enter only through

J. P. Rice and B. C. Johnson: Optical Technology Division, National Institute of Standards and Technology, Gaithersburg, MD 20899, USA.

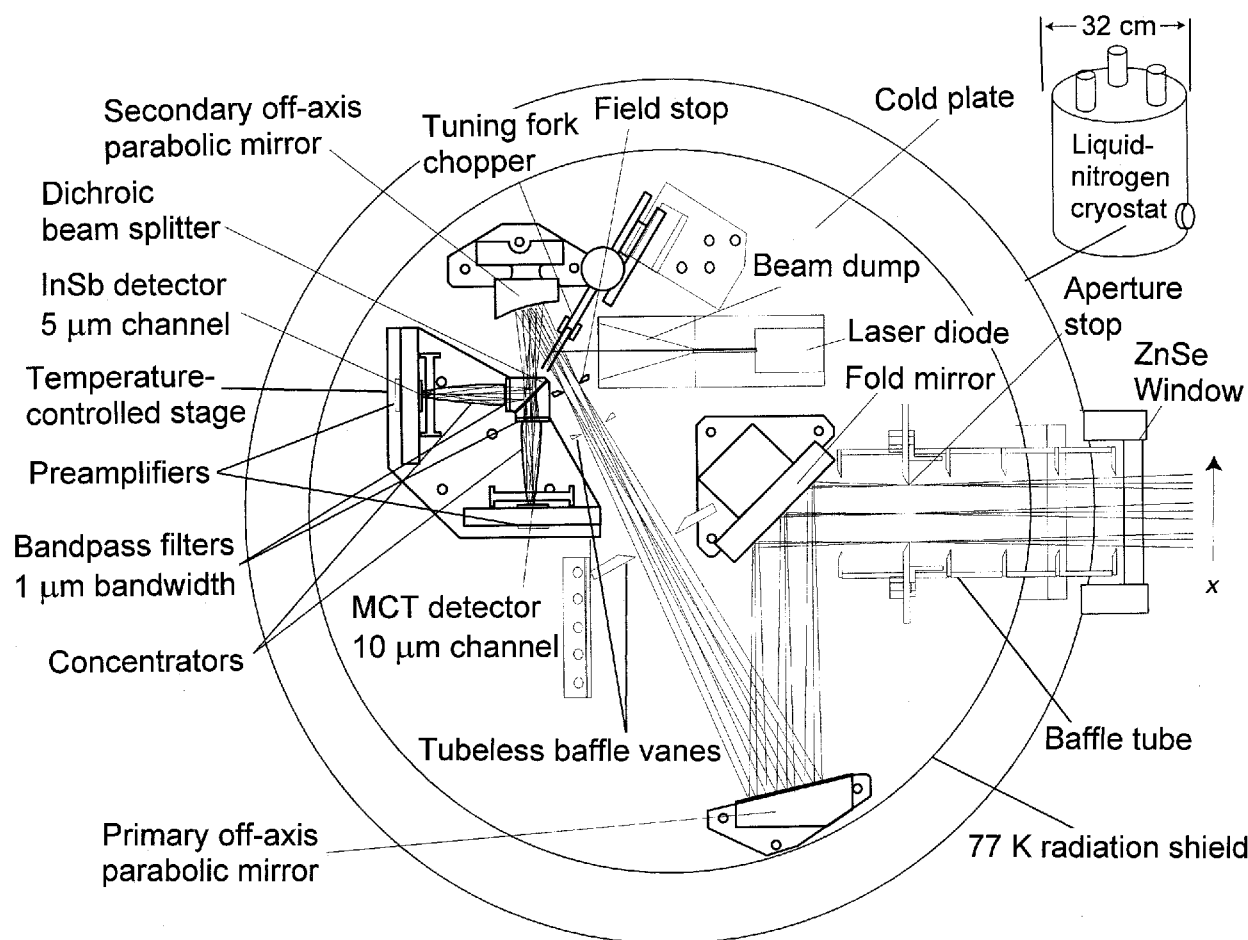


Figure 1. Optical layout of the TXR, showing the ray trace for viewing a source in radiance mode.

one hole facing the cryostat window. Thus, except for the cryostat window, all internal TXR components are under vacuum, are cooled by direct conduction to below 80 K, and are surrounded by surfaces having a temperature of nominally 77 K.

Light from the source enters the TXR through a plane-parallel ZnSe cryostat window (Figure 1). It penetrates the radiation shield through a four-vane baffle tube preceding a 2 cm diameter aperture that serves as the aperture stop. Then the light passes a single-vane post-aperture-stop baffle tube and reflects off the flat-fold mirror and the primary off-axis parabolic mirror. After passing through two tubeless baffle vanes, the light passes through a nominally 6 mm diameter aperture that serves as the field stop. The field stop, in combination with the aperture stop and the primary mirror, defines a beam that is 2 cm in diameter and has 2° field-of-view as measured at the aperture stop. This beam is chopped by the tuning fork chopper. The light that traverses the chopper when its vanes are open reflects off the secondary off-axis parabolic mirror and is directed towards the filter-detector stage. Both the primary and secondary off-axis parabolic mirrors have their foci at the field stop. Thus, collimated light entering the TXR would be focused by the

primary parabolic mirror to a point at the field stop and recollimated by the secondary parabolic mirror. However, when the TXR is used to measure the radiance of an extended area source, which is the intended application, both the aperture stop and field stop are overfilled spatially with light and the beam cannot be considered collimated. Instead, the beam reaching the filter-detector stage has a divergence full-angle of about 14° , and so is roughly $f/4$.

When the beam reaches the filter-detector stage, it is split spectrally by the dichroic beam splitter. This optic reflects light having wavelengths shorter than $5.5 \mu\text{m}$, and transmits light having wavelengths longer than $7 \mu\text{m}$. The reflected light is incident on the $5 \mu\text{m}$ centre-wavelength bandpass filter and is concentrated onto the InSb detector. Meanwhile, light transmitted through the dichroic beam splitter is incident on the $10 \mu\text{m}$ centre-wavelength bandpass filter and concentrated onto the MCT detector. The non-imaging concentrators used are the θ_i/θ_o design described elsewhere [10]. To minimize electrical pickup, each detector has a custom-designed cold transimpedance amplifier mounted not more than 1 cm away, so that preamplified, millivolt-level signals are available from the TXR cryostat.

The main purpose of the tuning fork chopper is to improve background subtraction and to enable ac measurements of the detector signals for improved signal-to-noise ratios. Under TXR operating conditions at 77.6 K, its chopping frequency is 43.551 Hz with a measured frequency stability of ± 0.002 Hz. During the phase of the chopping cycle when the gold-coated chopper vanes obstruct the beam, they reflect the light into the beam dump. The beam dump absorbs this unwanted light, sinking its thermal load into the cold plate. The beam dump also houses a laser diode that serves as the TXR alignment source. When this is turned on, its visible-red laser light reflects off the front of the chopper vanes and follows the optical path in reverse order to that described above, emerging on-axis from the TXR cryostat window. This beam can be used to align the TXR with respect to the source under test. A special constant-current driver circuit is used so that the laser diode operates at any temperature between 300 K and 77 K.

The dichroic beam splitter, bandpass filters, concentrators, detectors, and the transimpedance preamplifiers are all mounted on a common copper stage, thermally linked to the cold plate through three brass spacers. The copper stage has an integrated electrical heater and a silicon-diode temperature sensor, which are used with a commercial temperature controller to maintain the stage at a temperature of nominally 78 K with a stability of about 1 mK. This is done to avoid instability resulting from the temperature dependences of the spectral transmission of the filters and the responsivity of the detectors.

3. Spectral characterization

For preliminary measurements of relative spectral responsivity, the TXR was mounted at the output of the monochromator at the NIST Infrared Spectral Comparator Facility (IR SCF) [11]. The $f/4$ beam from the monochromator was focused to a nominally 2 mm spot at the centre of the TXR aperture stop. In this geometry, the aperture stop is underfilled but the field stop is overfilled. An argon-arc source at 90 A current was chopped before the input to the monochromator at 41 Hz by a rotating blade chopper. The TXR chopper was turned off during the spectral tests; its vanes are open in the off position. The resulting signals, detected with a lock-in amplifier, were measured as a function of monochromator wavelength. The data were divided by the known relative spectral distribution of flux at the output of the monochromator to provide a measure of the relative spectral responsivity (Figure 2). In the IR SCF, the relative spectral distribution of flux at the output of the monochromator for a given set of arc source and monochromator parameters can in principle be measured nearly simultaneously with the detector under test (the TXR) by using a silicon bolometer having a

well-characterized, nearly flat spectral response [11]. However, for the preliminary measurements reported here, the relative spectral distribution of flux at the output of the monochromator was determined instead by folding together data from previous measurements of the throughput of the monochromator and the spectral radiance of the arc source. In Figure 2, the low signal-to-noise ratio for the 10 μm Channel can be improved greatly in future measurements by changing the grating in the monochromator to one that is better optimized for 10 μm and is known to provide more power. Note that this is an end-to-end spectral measurement of the entire TXR radiometer. For comparison, Figure 2 also shows the relative filter transmittance of each filter. This shows that the end-to-end relative spectral responsivity, which includes the relative spectral transmission, reflectance, and responsivity of the components along the TXR optical path, is dominated primarily by the relative filter transmittance.

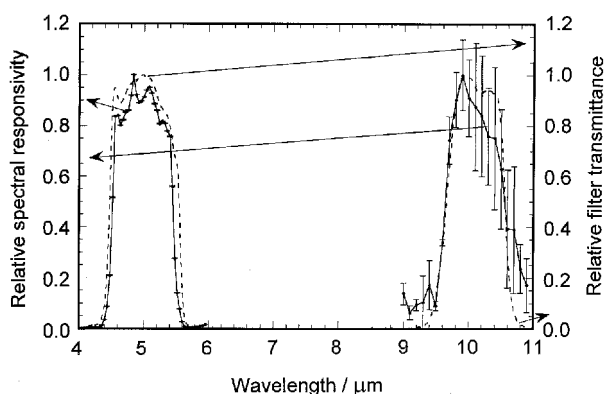


Figure 2. Relative spectral responsivity of the TXR channels as measured in the NIST Infrared Spectral Comparator Facility (solid lines with error bars), compared with the relative filter transmittance (dashed lines without error bars). Note that all four curves are individually peak-normalized so that their shapes can be compared.

4. TXR viewing a water-bath black-body source

For characterizations of detector signal versus time and detector signal versus black-body temperature, the TXR was mounted with its aperture stop a distance of 37.3 cm from the 10.8 cm diameter exit aperture of an ambient water-bath black-body source used for routine infrared calibrations at the NIST [12]. In this geometry, for which the TXR is specifically designed, both the aperture stop and the field stop of the TXR are overfilled, so the measurements can be interpreted in terms of band-integrated radiance. With the TXR internal chopper on, the preamplified detector signals were nearly square waves with 60 % duty cycle, and 10 % to 90 % rise and fall times of $1.45 \text{ ms} \pm 0.02 \text{ ms}$. For each channel, the chopped signal was measured simultaneously by individual digital lock-in amplifiers and the dc magnitude of the lock-in amplifier signal at the chopping frequency was recorded. To define

a narrow electrical bandwidth about the chopping frequency for optimum noise suppression, a post-detection lock-in time constant of 1 s was used for both TXR channels. At each black-body temperature, the data-acquisition software for the TXR recorded the black-body PRT reading and the magnitude of the signals from the two TXR channels. For the purposes of this paper, the PRT reading is used to define the black-body temperature.

Currently, as for the EOS sources, the radiance temperature scale for this black-body source is established through contact thermometry, though comparisons with a gallium-point black-body source have been made. Also, its temperature range is limited to between 278 K and 353 K. However, it provides a stable source useful for detector stability and preliminary temperature-dependence studies. For calibration over a wider temperature range, tests will be performed with the TXR viewing the large-area black body (LABB) source in the Medium Background Infrared (MBIR) facility at the NIST [13]. Also, the LABB source will have a radiance temperature calibration against the NIST detector-based radiometric scale [14]. For the purposes of this paper, signals are plotted against the temperature indicated by the calibrated PRT, which is in contact with the water-bath. Such data are shown in Figure 3. Each data point was determined by averaging drift-free detector signals for at least 20 min, during which the PRT temperature was stable to within ± 0.18 mK or better.

For each channel, the data in Figure 3 were fitted to an effective wavelength approximation of the Planck radiation law as a function of temperature:

$$S(T) = a \frac{c_1}{\lambda_0^5 \{\exp(c_2/\lambda_0 T) - 1\}} + b. \quad (1)$$

Here, S is the detector signal (at the output of the lock-in amplifier), T is the black-body temperature (taken as equal to the PRT temperature in the present approximation), c_1 and c_2 are the first and second radiation constants, λ_0 is the centre wavelength of each channel, and a and b are the slope and offset that

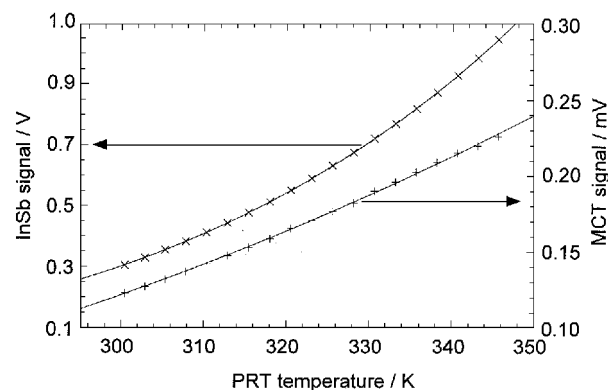


Figure 3. TXR signals versus PRT temperature for the TXR viewing a water-bath black-body source. The lines are fits to an effective wavelength model.

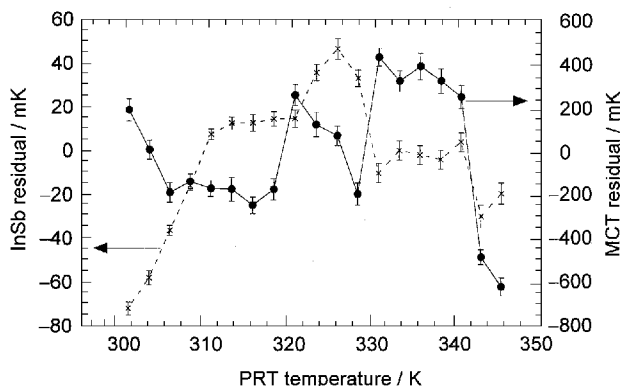


Figure 4. Residuals (data – fit) of the fits shown in Figure 3. The error bars are the standard deviation of the TXR signals with the source stabilized at each temperature, and thus indicate the precision of the TXR for measuring radiance temperature. The lines are a guide for the eye.

were used as the two fitting parameters. For the fits shown in Figure 3, $\lambda_0 = 5 \mu\text{m}$ for Channel 1 and $\lambda_0 = 10 \mu\text{m}$ for Channel 2. The residuals of the fits are shown in Figure 4. The fact that the residuals are greater than the measurement precision is an indication that perhaps a better model, incorporating the actual relative responsivity (Figure 2), should be used.

The 1σ noise-equivalent temperature of the TXR channel at 300 K is about 3 mK (error bars on Figure 4). This is a factor of ten better than the desired value of 0.01 %. With such precision, systematic effects such as the size-of-source effect and cavity loading will probably dominate the uncertainty for the EOS comparisons. However, the low noise will improve the precision of the characterizations required to make corrections for these effects. For the $10 \mu\text{m}$ channel, the noise is about 50 mK, which is just below 0.02 %. Thus, the radiance temperature determined from this channel will be less precise than that from the $5 \mu\text{m}$ channel, but is still consistent with the ability to verify the typical 0.05 % uncertainty estimate for the EOS black bodies.

5. Spatial characterization

For point-spread response measurements in an ambient background, a soldering iron having a 2.5 mm diameter tip was mounted on an x - y scanning stage with its tip aligned along the TXR optical axis. The TXR chopped signals from Channels 1 and 2, as measured on the lock-in amplifiers, were recorded via computer-controlled data-acquisition software as the heated soldering iron was translated. It was necessary to subtract the ambient temperature background and to correct for drift of the scene. An example of the corrected data is shown in Figure 5. The solid curve accounts for the gradual roll-off near the edge of the field-of-view according to the following model. The aperture stop has a radius of $r_1 = 1$ cm. The half-angle of the TXR field-of-view is, from ray tracing, 1.07° . Thus, only the cone of light from

the soldering-iron tip within this half-angle is within the TXR field-of-view. The projection of this cone onto the plane of the aperture stop forms a circle of radius $r_2 = 2.2$ cm for the position of the scanning plane of the soldering iron (118 cm from the aperture stop) used in the measurements. The radiant flux reaching the detectors is proportional to the overlap area of the circle of radius r_1 and the circle of radius r_2 , as their centres are displaced. The analytical function for the overlap area of two circles is given in [15]. The only fitting parameter for the curve was the signal amplitude at the plateau where the two circles completely overlap.

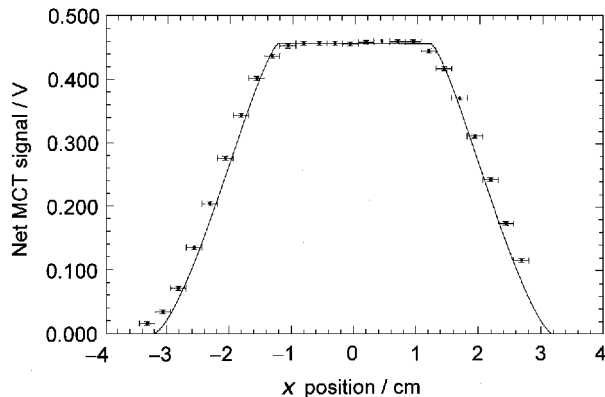


Figure 5. An example of point-spread response data for the MCT channel measured by translating a heated soldering iron in the x direction (see Figure 1) across the centre of the TXR field-of-view. The circles are the background-subtracted and drift-corrected data. The position error bars indicate the soldering-iron tip diameter, while the signal error bars indicate the standard deviation of fifteen readings at each position. The solid line is a fit to the model described in the text.

6. Conclusion

A version of the TXR has been built and characterized using state-of-the-art NIST ambient-infrared facilities. The final version is essentially unchanged, except that it is built into a thermal/vacuum-chamber-compatible cryostat. The contribution of random uncertainty to the total measurement uncertainty is compatible with the goal of enabling NIST-traceable radiometric comparisons of EOS black-body sources with a radiance temperature uncertainty better than the predicted uncertainty of the sources.

Acknowledgements. We thank G. Eppeldauer, A. L. Migdall, and F. J. Lovas for assistance with the ambient-infrared characterization facilities. This work was supported in part by the NASA EOS Project Science Office (S-41365-F).

References

- Butler J. J., Johnson B. C., Organization and Implementation of Calibration in the Earth Observing System (EOS) Project – Part 1, *The Earth Observer*, 1996, **8**(1), 22-27.
- Butler J. J., Johnson B. C., Calibration in the Earth Observing System (EOS) Project – Part 2: Implementation, *The Earth Observer*, 1996, **8**(2), 26-31.
- Rice J. P., Johnson B. C., A NIST Thermal Infrared Transfer Standard Radiometer for the EOS Program, *The Earth Observer*, 1996, **8**(3), 31-35.
- Guenther B., Barnes W., Knight E., Barker J., Harnden J., Weber R., Roberto M., Godden G., Montgomery J., Abel P., MODIS Calibration: A Brief Review of the Strategy for the At-Launch Calibration Approach, *J. Atmos. Oceanic Tech.*, 1996, **13**, 274-285.
- Lee R. B., Barkstrom B. R., Smith G. L., Cooper J. E., Kopia L. P., Lawrence R. W., Thomas S., Pandey D. K., Crommelynck D. A. H., The Clouds and the Earth's Radiant Energy System (CERES) Sensors and Preflight Calibration Plans, *J. Atmos. Oceanic Tech.*, 1996, **13**, 300-313.
- Ono A., Sakuma F., Arai K., Yamaguchi Y., Fujisada H., Slater P. N., Thome K. J., Palluconni F. D., Kieffer H. H., Preflight and In-Flight Calibration Plan for ASTER, *J. Atmos. Oceanic Tech.*, 1996, **13**, 321-335.
- Jarecke P. J., Folkman M. A., Hedman T. R., Frink M. E., Clouds and the Earth's Radiant Energy System (CERES): Long-wave Calibration Plan and Radiometric Test Model (RTM) Calibration Results, *Metrologia*, 1993, **30**, 223-230.
- Parr A. C., A National Measurement System for Radiometry, Photometry, and Pyrometry Based Upon Absolute Detectors, *NIST Tech. Note 1421*, 1996.
- Rice J. P., Lorentz S. R., Datla R. U., Vale L. R., Rudman D. A., Lam Chok Sing M., Robbes D., Active cavity absolute radiometer based on high- T_c superconductors, *Metrologia*, 1998, **35**, 289-293.
- Rice J. P., Zong Y., Dummer D. J., Spatial Uniformity Comparison of Two Non-Imaging Concentrators, *Opt. Eng.*, 1997, **36**, 2943-2947.
- Migdall A. L., Eppeldauer G. P., Cromer C. L., IR detector spectral responsivity calibration facility at NIST, *Proc. SPIE*, 1994, **2227**, 46-53.
- Fowler J. B., A Third Generation Water Bath Based Blackbody Source, *J. Res. Natl. Inst. Stand. Technol.*, 1995, **100**, 591.
- Fowler J. B., Johnson B. C., Rice J. P., Lorentz S. R., The new cryogenic vacuum chamber and black-body source for infrared calibrations at the NIST's FARCAL facility, *Metrologia*, 1998, **35**, 323-327.
- Datla R., Croarkin M., Parr A. C., Cryogenic blackbody calibrations at the National Institute of Standards and Technology Low Background Infrared Calibration Facility, *J. Res. Natl. Inst. Stand. Technol.*, 1994, **99**(1), 77-87.
- O'Shea D. C., *Elements of Modern Optical Design*, New York, John Wiley & Sons, 1985, 104.